Research Article Vol. 57, No. 21 / 20 July 2018 / Applied Optics 6017

Modeling of an active terahertz imaging system in brownout conditions

Clotilde Prophète,[1,2,*] Romain Pierrat,[1,2] Hervé Sik,[3] Emmanuel Kling,[3] Rémi Carminati,[1,2] and Julien de Rosny[1,2]

[1]ESPCI Paris, PSL Research University, Institut Langevin, 1 rue Jussieu, F-75005 Paris, France
[2]CNRS, Institut Langevin, 1 rue Jussieu, F-75005 Paris, France
[3]Safran Electronics & Defense, 100 avenue de Paris, 91344 Massy, France
*Corresponding author: clotilde.prophete@espci.fr

Received 28 March 2018; revised 18 June 2018; accepted 18 June 2018; posted 19 June 2018 (Doc. ID 327111); published 16 July 2018

We present a theoretical evaluation of a subterahertz (subTHz) system to image through a scattering medium composed of scatterers of sizes close to the wavelength. We specifically study the case of sand grain clouds created by helicopter rotor airflow during landing in arid areas. The different powers received by one pixel of a matrix made of subTHz sensors are identified. Photometric and antenna-based sensors are considered. Besides the thermal contribution to the noise, we focus our attention on the radiation backscattered by the brownout. It appears that a configuration where the source and the camera are distant is the most promising configuration and is realistic for embedded systems.

OCIS codes: (110.0113) Imaging through turbid media; (290.1350) Backscattering; (110.6795) Terahertz imaging; (010.5630) Radiometry; (070.7345) Wave propagation.

https://doi.org/10.1364/AO.57.006017

1. INTRODUCTION

During landing or takeoff of helicopters in arid areas, rotor airflow generates a cloud of sand. This cloud, called *brownout*, can be tens of meters thick and cause low-to-zero visibility. As a consequence, the pilot may be disoriented, and accidents may occur. Thus, finding solutions to reduce the collision risk is becoming a strategic research axis for civilian as well as military purposes. To that end, different approaches are considered.

One of them consists in finding the best landing zone where limited brownout occurs based on the analysis of visible and infrared satellite imagery [1]. The most significant indicator is given by the normalized difference vegetation index. However, the method strongly limits the number of landing areas.

Another approach lies in better training of the pilot with realistic flight simulators. A numerical simulation of brownouts generated by helicopters has been developed [2]. This simulation tool includes the rotorcraft wake model, the particle entrainment model, the particle transport model, and the visual obscuration model. The pilot training is, however, relevant only when the runway visual range (RVR) is not too degraded. Using the same kind of global numerical approach, Swanson [3] has estimated RVR for different helicopter types, sand grain diameters, and wind speeds. It appears that the RVR is too small for most recent heavy helicopters.

For these reasons, the most promising solution is to develop driver's vision enhancer (DVE). Basically, a DVE sensor is made of three parts: sensors, signal processing, and synthetic vision [4]. Some solutions are based on a real-time 3D optical terrain mapping when the rotorcraft is approaching. When the brownout disturbs the pilot, a 3D terrain reconstruction takes place. This method, however, assumes that no obstacle penetrates the landing area after the brownout rising.

To get a better penetration through brownout, some systems are based on infrared lidar. However, they are only operational for mild degraded visibility [5] because of the strong scattering of infrared through brownout. Radar DVE, which works between Ku and subterahertz (subTHz) bands, suffers less from scattering because the wavelength is larger than the particle sizes. Nonetheless, these systems do not provide a sufficient resolution at low frequency. Furthermore, embedded systems must be light and compact, and radar with such properties may be difficult to implement. DVE working in the subTHz range is the best trade-off between penetration and resolution. Particularly, for a couple of years, subTHz technology has made rapid progress leading to solutions that could not be considered beforehand. For instance, an embedded device with four sensors working at 94 GHz has been implemented as a landing aid system to estimate the drift and height of the aircraft [6,7]. More recently, a laboratory test of a mechanical

radar prototype operating between 300 and 330 GHz has been performed without brownout [8].

However, the SWAP-C (size, weight, power, cost) of subTHz radar is still very high [4]. A subTHz imaging system seems to be much more realistic because the operation principle is far less complex. Based on this principle, prototypes made of dozens of pixels and working at 77 and 95 GHz have been developed [9,10]. Nevertheless, those systems are still quite large to get a sufficient resolution. Lately, pixels working around 300 GHz [11,12] have been developed and seem promising to reduce SWAP-C. One can overcome the technological difficulty of getting a high-resolution array of subTHz sensors by using a single-pixel camera with a coded aperture instead [13]. A full passive imaging system has been tested [14] with a dual-polarization W-band (75 to 110 GHz) radiometer. If an obstacle is placed in the field of view, one can evaluate the detection efficiency due to the temperature contrast between the obstacle and the background. For the horizontal polarization, one can detect an obstacle with a temperature contrast between 15 and 25 K. The brownout generated by a small helicopter only lowers this contrast by 2% (attenuation factor of only 1.14 dB/km). As one can see, a key parameter of subTHz imaging through brownout is the wave attenuation due to absorption and scattering. Several measurements have been performed in a controlled environment. In a 3-m-long wind tunnel [15], losses smaller than 0.4 dB have been observed between 94 and 217 GHz with a sand density ranging between 170 mg/m^3 and 3379 mg/m^3. More recently, at higher frequencies (between 446 and 631 GHz), attenuations ranging between 1 and 3 dB have been reported in a 15-m-long tunnel [16].

In parallel to these technological and experimental developments, one challenge is to develop models for the subTHz propagation through brownout. Basically, they result from the coupling between models predicting aerosol flow models and THz wave attenuation. The aerosol dynamic model is of course strongly linked to the airflow generated by the rotating blades of helicopters [17]. The attenuation is concomitantly due to the molecular absorption by the various air components [18,19] and the scattering by the aerosols. It has been recently shown that the extinction is dominated by scattering under 500 GHz [20]. Consequently, in that frequency range, the wave attenuation, or the visibility, varies dramatically from one arid area to another and from one helicopter type to another. A package called laser environmental effects definition and reference (LEEDR) is currently being developed to predict the local visibility of approximately 400 sites. It is based on the fusion of all the aforementioned models, a climatological database, and aerosol models [21,22].

However, to the best of our knowledge, subTHz electromagnetic wave propagation through brownout has not attracted much attention. Particularly, active systems, for which the scene is illuminated by a subTHz source, have not been much studied. Such systems are *a priori* promising, as they were proven efficient for other scattering media in the infrared [23,24]. In this work, we present an advanced modeling of an active subTHz imaging system to assess its performance. We focus our study on a wide frequency range between 94 and 940 GHz, corresponding to wavelengths between 319 μm and 3.19 mm. Based on the analysis of the radiative transfer equation (RTE) that models the propagation of THz radiance, we show that within this frequency band, an imaging system is able to detect a target that is at least 30 m away. To reach this conclusion, the paper is divided into five sections, including this introduction.

In the next section of the paper, we state the problem with the definition of the imaging system and a typical brownout configuration. In Section 3, the different aspects of the model are described: signal attenuation, atmosphere absorption, etc. A large part is dedicated to the noise backscattered by the brownout. In Section 4, we present the results deduced from the model for various parameters. Most of the analytical results are compared with Monte Carlo simulations [25,26]. In the last part of Section 4, a complete balance between the different powers received by a pixel of the imaging system is presented. In Section 5, we discuss the results in order to hold out a functional configuration for a subTHz active imaging system.

2. PROBLEM STATEMENT

In order to image through brownouts, we choose to use a powerful monochromatic source to produce the incident field. As the emissivity variation can be quite small in the subTHz range (less than 10%) [14], a passive imaging system may not be efficient enough. An active system is not limited by such an effect because the signal depends on the albedo (intensity reflection coefficient) that equals $1 - e$, e being the emissivity. In other words, a low-contrast scene in emissivity corresponds to a high one in reflection.

We assume the source emits a uniform radiance in a cone of half-aperture θ_0. To get a real-time and robust imaging system, the detection system is composed of a matrix of detectors (pixels). To keep a compact and power efficient system, the matrix is composed of 640 pixels × 480 pixels. Two different kinds of pixels are studied: photometric detectors, such as microbolometers, or electromagnetic antennas. The schematic view of the imaging system is represented in Fig. 1.

The detection system is located at a distance d_{s-d} from the source and at the focus of a converging lens. In Fig. 1, only one pixel is drawn. The brownout is assumed to be separated by a distance z_0 from the pupil. The thickness of the brownout is D. The scene to be imaged is located at a distance $D + z_0$ from the imaging system. We assume the imaged scene is Lambertian (nonspecular reflection), and its albedo is A_g. The optimal working frequencies are chosen within the several transmission windows of the subTHz spectrum (94, 140, 220, 350, 410, 680, 850, 940 GHz) [27].

The signal is the power backscattered by the scene to be imaged. On top of that, the source emission generates a noise as it is backscattered by the sand grains of the brownout. Finally, the pixel also receives noise due to thermal radiation from the ground and the sky.

3. MODEL

Our goal is to evaluate the performance of the imaging system. After evaluating the attenuation of THz waves by the atmosphere and the brownout, we estimate the radiances of signal

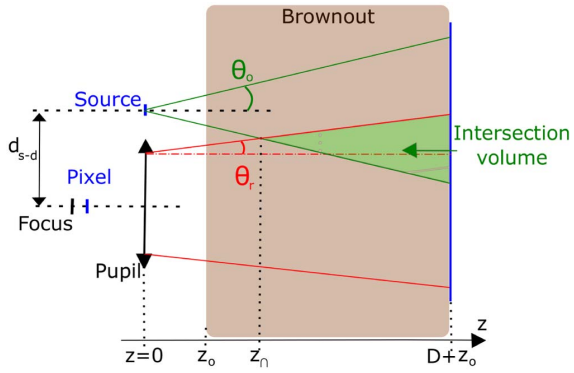

Fig. 1. Schematic view of the active imaging system. The source of half-aperture θ_0 illuminates the scene that is located at a distance $D + z_0$ from the imaging system. The detection system consists in a matrix of pixels located in the image plane of the optical system, which pupil is located at $z = 0$. The half-aperture of one pixel is θ_r. Only the pixel centered on the optical axis is represented. The distance between the axes of the source and the optical system is d_{s-d}. The brownout is in contact with the ground, and its thickness is D. The volume from which the backscattered noise hails is shown in green. It is the intersection between the cones of illumination and detection.

and noises that are incident on the pupil of the optical system. Then, for each contribution, we deduce the power that is collected by the pixel centered on the optical axis. Both cases of the photometric pixel and antenna are presented.

A. Attenuation of THz Waves

The attenuation is due to two concomitant effects: the absorption of the different gas components of the atmosphere and the scattering by sand grains. Assuming that Beer–Lambert law governs the attenuation, the total extinction mean free path (ℓ_{tot}), i.e., distance after which the incident wave is attenuated by a factor $1/e$, is given by

$$\frac{1}{\ell_{\text{tot}}} = \frac{1}{\ell_{\text{atm}}} + \frac{1}{\ell_{\text{sca}}} + \frac{1}{\ell_{\text{abs}}}, \tag{1}$$

where ℓ_{atm}, ℓ_{sca}, and ℓ_{abs} are the absorption mean free path in air, the scattering, and the absorption mean free paths of the sand grain suspension, respectively.

B. Atmosphere Absorption

The absorption due to atmospheric gazes depends on many parameters: temperature, pressure, and water vapor density. The radio-communication sector of the international telecommunication union provides a recommended model [27] that is valid between 1 GHz and 1 THz. At sea level, the attenuation is dominated by absorption lines of water vapor and increases with frequency. Consequently, the absorption strongly depends on air humidity. In the following, we choose the standard atmosphere with 44% relative humidity, which corresponds to an arid zone.

C. Brownout Attenuation

Concerning the brownout, it is challenging to choose a model, as brownouts are different from one area to another, and one helicopter to another. We assume the sand is made of spherical silica particles. Between 94 and 940 GHz, the silica refractive

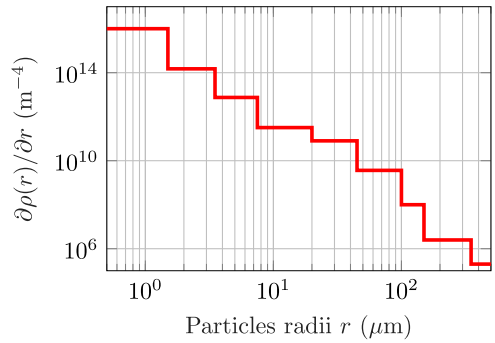

Fig. 2. Distribution of brownout particle density with respect to particles' radii for a large military helicopter [28].

index is almost constant and equals 1.96. The distribution in size and concentration of the brownout particles has been measured for different helicopters [28]. In Fig. 2, an averaged density per unit of particle radii is represented. This distribution follows approximately a Marshall–Palmer law, which was originally designed for rain droplets. The particle density decreases with respect to the particle radius from 1×10 m^{-3} to 100 m^{-3}. The particle density in brownout is low so that the effect of absorption by silica is negligible. As a result, we can neglect the absorption mean free path, ℓ_{abs}, of the silica particles.

The scattering mean free path due to the brownout is given by

$$\frac{1}{\ell_{\text{sca}}} = \int \frac{\partial\rho(r)}{\partial r}\sigma_{\text{sca}}(r)\mathrm{d}r, \tag{2}$$

where $\sigma_{\text{sca}}(r)$ is the extinction cross section of a particle of radius r and $\partial\rho(r)/\partial r$ the particle density per unit of radius. Assuming sand grains are spherical silica particles, the scattering efficiency $\sigma_{\text{sca}}(r)/\pi r^2$ can be estimated with the Mie theory [29]. The scattering efficiency versus the particle radius for one silica sphere is shown in Fig. 3 for three frequencies of interest. For the lowest frequency, the scattering efficiency follows the Rayleigh approximation, as the wavelength (3.19 mm) is far bigger than the radii. For higher frequencies, Mie resonances come up.

In Fig. 4, the extinction mean free path, ℓ_{tot}, is plotted in the subTHz frequency range. We observe that for this particle

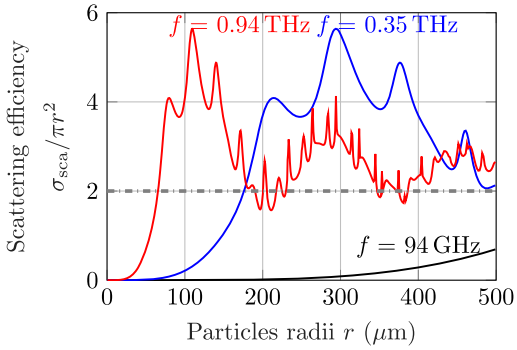

Fig. 3. Scattering efficiencies for three frequencies (94 GHz, 0.35 THz, and 0.94 THz) for silica spheres with index of refraction of 1.96.

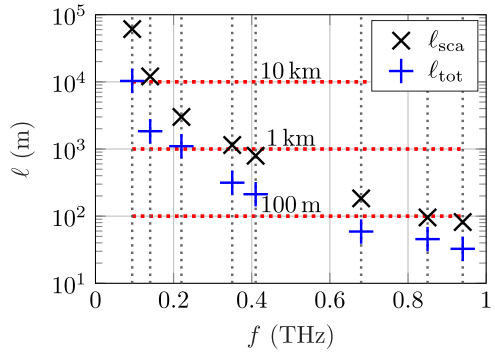

Fig. 4. Scattering and extinction mean free paths for a brownout made of silica spheres deduced from Eqs. (1) and (2) and Mie scattering model for a brownout distribution shown in Fig. 2.

distribution, the extinction is driven by the atmosphere absorption rather than scattering. Indeed, ℓ_{sca} is at least 4 times larger than ℓ_{tot}.

To have a first evaluation of the efficiency of a subTHz imaging system, we can compare its performance with the pilot's vision without any imaging systems. To that end, we also determine the attenuation in the visible spectrum. In the visible range, the particle radius r is much larger than the wavelength. As a consequence, the extinction cross section equals $2\pi r^2$, i.e., the extinction efficiency equals 2. In this spectral range, the mean free path of the brownout generated by the large helicopter is $\ell_{pilot} = 10$ m. This mean free path is directly linked to the visibility defined by Koschmieder's law [30,31]. This law defines the visibility as the distance at which the minimum contrast is identifiable by an observer:

$$V_{pilot} = -\ell_{pilot} \log C_t, \tag{3}$$

where C_t is the contrast that equals 0.05. Thus, a mean free path ℓ_{pilot} of 10 m corresponds to a visibility V_{pilot} of 30 m.

Now that the attenuation of subTHz waves due to the environment (i.e., atmosphere and brownout) has been evaluated, we determine the radiances reaching the pupil of the system in the following sections. First, we estimate the signal backscattered by the scene and the noise backscattered by the suspended sand grains. Then, we look at the thermal radiation contributions. The backscattered radiance due to the scene and the brownout are deduced from the RTE, which is described in Appendix A.

D. Signal Backscattered by the Scene

In Appendix C, we show that the expression of the signal radiance backscattered by the scene, at the receiver, is given by

$$L_s^r = \frac{A_g G_s(\hat{\mathbf{z}}) P_0}{4\pi^2 (D+z_0)^2} \exp\left(-\frac{2(D+z_0)}{\ell_{tot}}\right), \tag{4}$$

where G_s, P_0, and are, respectively, the emission antenna gain and the source power. The reflection by the surface to image is assumed perfectly Lambertian with an albedo A_g. Unit vector $\hat{\mathbf{r}}$ points toward the direction viewed by the pixel.

In the following, we are going to deal with a source with a constant radiance inside a cone of half-angle θ_0. In this case, the antenna gain is given by

$$\begin{cases} G_s(\hat{\mathbf{r}}) = \frac{2}{1-\cos\theta_0} & \text{if } \hat{\mathbf{r}}\cdot\hat{\mathbf{r}}_0 \geq \cos\theta_0 \\ G_s(\hat{\mathbf{r}}) = 0 & \text{everywhere else,} \end{cases} \tag{5}$$

where $\hat{\mathbf{r}}_0$ is the direction of the main emission lobe.

Thus, for $\hat{\mathbf{r}}\cdot\hat{\mathbf{r}}_0 \geq \cos\theta_0$,

$$L_s^r = \frac{A_g}{\pi} \frac{P_0}{2\pi(1-\cos\theta_0)} \frac{\exp(-2(D+z_0)/\ell_{tot})}{(D+z_0)^2}. \tag{6}$$

E. Noise Backscattered by the Brownout

The brownout particles backscatter the incident subTHz wave emitted by the source. This contributes to the noise received by the pixel. Therefore, it is crucial to estimate the backscattered power level. To that end, we present a semianalytical solution based on a single-scattering approximation. This approximation is in accordance with the fact that the subTHz imager operates at a frequency where the scattering mean free path is larger than the brownout thickness. On the other hand, we neglect the combination of a scattering event by a particle and backscattering by the Lambertian scene. Based on these approximations, we show in Appendix D that the scattered radiance L_d by the brownout is the solution of the following RTE:

$$\hat{\mathbf{u}}\cdot\nabla L_d(\mathbf{r},\hat{\mathbf{u}}) + \frac{1}{\ell_{tot}} L_d(\mathbf{r},\hat{\mathbf{u}}) = S_d(\mathbf{r},\hat{\mathbf{u}}), \tag{7}$$

where the source term S_d is defined as

$$S_d(\mathbf{r},\hat{\mathbf{u}}) = \frac{1}{4\pi\ell_{sca}} \int_{4\pi} p(\hat{\mathbf{u}}'\to\hat{\mathbf{u}}) L_s(\mathbf{r},\hat{\mathbf{u}}')\mathrm{d}\hat{\mathbf{u}}'. \tag{8}$$

The development of the incident radiance L_s generated by the emitting antenna is performed in Appendix B. The phase function $p(\hat{\mathbf{u}}'\to\hat{\mathbf{u}})$ accounts for the scattering by the brownout from direction $\hat{\mathbf{u}}'$ to direction $\hat{\mathbf{u}}$. Introducing the Green function $\mathcal{G}_0$, solutions of Eq. (7) can be advantageously written as

$$L_d(\mathbf{r},\hat{\mathbf{u}}) = \int_V \mathcal{G}_0(\mathbf{r}-\mathbf{r}',\hat{\mathbf{u}}) S_d(\mathbf{r}',\hat{\mathbf{u}})\mathrm{d}\mathbf{r}'. \tag{9}$$

The complete derivation of the radiance based on this integral equation is performed in Appendix D. The final expression of L_d is given by Eq. (D7).

F. Thermal Radiation

The other source of noise is thermal radiation that hails from the sky and the ground. To evaluate their contributions, we use the Planck function B_f. The sky presents an equivalent temperature T_s that depends on frequency and the considered atmosphere [32]. For the ground, we assume an albedo $A_g = 0.1$ and a temperature $T_g = 40$°C. The values do not change much for temperatures between 25°C and 45°C.

In order to determine the radiance received by the imaging system, we integrate the Planck function over the bandwidth of the detector Δf and centered on the working frequency f_0. The thermal noise radiance per hertz from the ground is given below:

$$L_g = (1 - A_g) \exp\left(-\frac{D}{\ell_{\text{tot}}}\right) B_f(T_g). \quad (10)$$

The factor $(1 - A_g)$ is the emissivity of the ground.

Then, the thermal noise radiance from the sky is

$$L_{\text{sky}} = A_g \exp\left(-\frac{2D}{\ell_{\text{tot}}}\right) B_f(T_s(f)). \quad (11)$$

The factor A_g hails from the backscattering of the sky radiation by the ground.

G. Power Received by a Pixel

All the radiances (i.e., backscattered signal and noise, thermal noise) reaching the pupil are known so that we can evaluate the power detected by the pixel centered on the optical axis. In this section, we evaluate this power for the different available technology: photometric pixel and antenna pixel. We present the results for the signal and the thermal noise, and the backscattered noise is evaluated separately.

1. Signal and Thermal Noise

The power detected by an antenna pixel is different from that detected by a photometric pixel. For a photometric pixel, the radiance is integrated over the pupil area S_{pup} with the solid angle seen by the pixel Ω_r. The detection half-aperture θ_r is a few milliradians so that $\Omega_r = \pi\theta_r^2$. The power of signal detected by a photometric pixel is finally

$$P_s^p = L_s^r S_{\text{pup}} \pi \theta_r^2, \quad (12)$$

with L_s^r given by Eq. (6). Assuming the scene to be imaged is at infinity, $\theta_r = a/(\sqrt{\pi} f)$, where a is the pixel size, and f is the focal length of the optical system.

In case of a pixel made of one small antenna, a different formalism applies. Similar to the source, the pixel is characterized by its gain G_r (that is generally different for the gain of the emitter). One can note that here, G_r takes into account the effect of the converging lens. As a consequence, the directivity is very narrow. The detected power is the integration, over the aperture solid angle, of the product between the irradiance L_s and the detection effective area of the antenna $(G_r(\hat{\mathbf{u}})\lambda^2/4\pi)$:

$$P_s^a = \int_0^{4\pi} L_s^r(\hat{\mathbf{u}}) \frac{G_r(\hat{\mathbf{u}})}{4\pi} \lambda^2 \cos(\theta_{\hat{\mathbf{u}}}) \mathrm{d}\hat{\mathbf{u}}. \quad (13)$$

Neglecting antenna losses and impedance mismatch, one can show that $\int_{4\pi} G_r(\hat{\mathbf{u}}) \mathrm{d}\hat{\mathbf{u}} = 4\pi$. With $\theta_r \ll 1$, $\cos\theta_{\hat{\mathbf{u}}} \approx \cos\theta_r \approx 1$. Besides, the distance between the source and the detection system is negligible compared to the distance between the imaging system and the scene and $\theta_r \ll \theta_0$. We finally get

$$P_s^a = L_s^r \lambda^2. \quad (14)$$

The same equations apply to compute the thermal power from the thermal radiance.

2. Backscattered Noise

In Appendix E, we show that the irradiance backscattered for one pixel is given by

$$E_d^r(\mathbf{r}) = \frac{P_0}{4\pi \ell_{\text{bs}}} \int_{4\pi} \frac{G_s(\hat{\mathbf{r}}')}{\cos(\theta_{\hat{\mathbf{r}}'})} [\mathcal{F}(\mathbf{r}, r_2(\hat{\mathbf{r}}')) - \mathcal{F}(\mathbf{r}, r_1(\hat{\mathbf{r}}'))] \mathrm{d}\hat{\mathbf{r}}'. \quad (15)$$

Here, $\ell_{\text{bs}} = 4\pi\ell_{\text{sca}}/p(\hat{\mathbf{u}} \to -\hat{\mathbf{u}})$, and the expression of $\mathcal{F}$ is provided in the Appendix E. Assuming small incident and reflected angles, an analytical solution similar to that developed in Ref. [33] is found (see Appendix E):

$$E_d(\mathbf{d}_{s-c}) = \frac{P_0 \Omega_{\text{pix}} G_s}{4\pi \ell_{\text{bs}}} \int_{z_0}^{D+z_0} \frac{S_\cap(z')}{S_{\text{pup}}} \times \frac{\exp\left(-\left(\sqrt{d_{s-c}^2 + z'^2} + z'\right)/\ell_{\text{tot}}\right)}{d_{s-c}^2 + z'^2} \mathrm{d}z', \quad (16)$$

with $z_\cap$ the coordinate on the z axis of the first point of intersection of the intersection volume and $S_{\text{int}}(z)$ the intersection area between the illuminating beam and the field of view of the pixel in the plane at coordinate z.

The backscattered power P_d^p (respect. P_d^a) of a photometric (respect. antenna) pixel due to the brownout is then deduced from Eq. (12) [respectively, (13)].

4. RESULTS

The analytical model is compared to a numerical simulation, in which a Monte Carlo method [25,26] is used to solve the RTE [Eq. (A1)] for the backscattered signal and backscattered noise. The Monte Carlo simulation consists in sending enough photons from the source of the imaging system so that the simulation converges to the RTE solution. The geometry of the Monte Carlo simulation is identical to the one of the analytical solutions (Fig. 1).

In the next two sections, we compare the radiances determined in Sections 3.D and 3.E to numerical simulations. Then, we present the thermal noise radiances evaluated in Section 3.F. Finally, with the expressions obtained in Section 3.G and for one set of parameters, we compare the complete power balances for an antenna and a photometric pixel.

A. Radiance of the Signal Backscattered by the Scene

The radiance of the backscattered signal is given by Eq. (6). Figure 5(a) shows the signal if the source aperture θ_0 is either 2.5° or 25°. In the first case, the radiance at the pupil is larger because the illumination is condensed in a small angle.

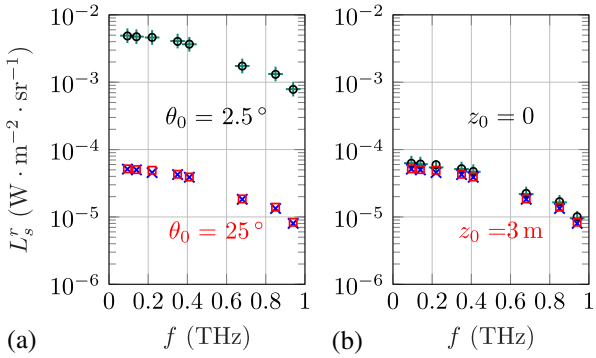

Fig. 5. Radiance of the backscattered signal—comparison between Monte Carlo simulation (+ and ×) and analytical model (○ and □). Parameters: $P_0 = 1$ W, $d_{s-c} = 0$, $D = 30$ m, $A_g = 0.1$. (a) Varying θ_0 ($z_0 = 3$ m) $0.28\% \le \varepsilon \le 7\%$; (b) varying z_0 ($\theta_0 = 25°$) $0.28\% \le \varepsilon \le 8\%$.

The second case ($\theta_0 = 25°$) is closer to real conditions, for which the system illuminates the full angle of view of the imaging system. We observe that the mismatch between the equation and the simulation does not exceed 7%. Eq. (6) gives, consequently, a satisfying determination of the signal.

In Fig. 5(b), θ_0 is settled at 25°, and the distance between the optical system and the brownout, z_0, evolves from 0 to 3 m. The radiance slightly increases when z_0 decreases, but they remain very similar. This is due to the fact that z_0 is negligible compared to the brownout thickness $D = 30$ m. As in Fig. 5(a), the mismatch between the analytical model and Monte Carlo simulation remains below 8%. In real brownout conditions, z_0 could reach a maximum of 5 m. Thus, we did not check the validity of Eq. (6) for larger values of z_0.

B. Radiance of the Noise Backscattered by the Brownout

The backscattered noise, as well as the backscattered signal, can be evaluated with the Monte Carlo simulation. We compare the results of this method with the analytical solution, which is obtained with Eq. (9). Similar to the backscattered signal, we study the evolution of the radiance for θ_0 varying from 2.5° to 25° [Fig. 6(a)], and for two values of z_0 [Fig. 6(b)]. In Fig. 6(a), the radiance is multiplied by 100 when θ_0 decreases by a factor of 10. This evolution is identical to that of the signal in Fig. 5(a). In both cases, this increase is directly due to the source power, which is more ($\theta_0 = 2.5°$) or less focused ($\theta_0 = 25°$).

Now, if we vary z_0 [Fig. 6(b)], the backscattered noise increases by a factor of 10, while the signal does not alter much [Fig. 5(b)]. As a consequence, the signal-to-noise ratio for the backscattered components highly depends on the distance z_0 that separates the imaging system from the brownout. The determination of this distance is crucial in real brownout conditions.

Concerning the mismatch between both resolution methods, it gets far higher for the backscattered noise than for the signal. It indeed reaches 38% in Fig. 6(a) and 27% in Fig. 6(b). These gaps can be explained by the backscattering factor $1/\ell_{\mathrm{bs}}$ that is taken proportional to the phase function in the direction opposite to the source.

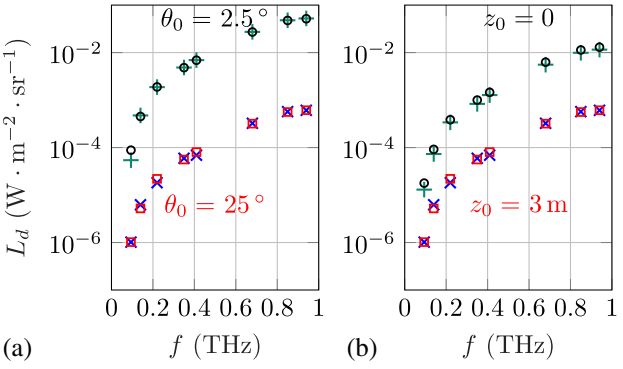

Fig. 6. Radiance of the backscattered noise—comparison between Monte Carlo simulations (+ and ×) and analytical model (○ and □). Parameters: $P_0 = 1$ W, $d_{s-c} = 0$, $D = 30$ m, $A_g = 0.1$. (a) Varying θ_0 ($z_0 = 3$ m) $0.18\% \le \varepsilon \le 38\%$; (b) varying z_0 ($\theta_0 = 25°$) $0.18\% \le \varepsilon \le 27\%$.

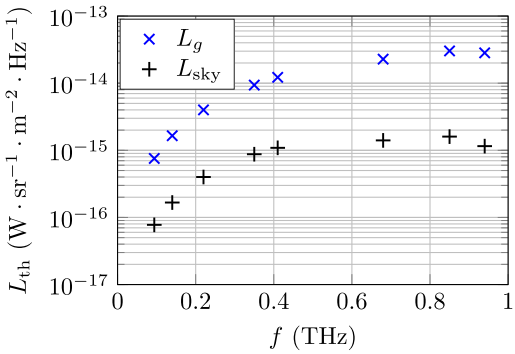

Fig. 7. Radiance of the ground, L_g, and the sky, L_{sky}, per hertz with respect to the frequency.

C. Radiance of the Thermal Noises

The radiance of the thermal noise per frequency unit is plotted in Fig. 7. As explained, thermal noises hail from the sky and the ground thermal radiations. However, the ground one dominates because the imaging system targets towards the ground and the pixel is only sensitive to the sky radiation reflected back by the ground. Due to the low albedo (0.1), its contribution is negligible compared to the thermal radiation of the ground, which has a high emissivity of about 0.9 ($1 - A_g$).

D. Complete Power Balance (Signal, Backscattered Noise, & Thermal Noise)

Since each contributing power has been introduced, we can now make the complete power balance for a photometric pixel [Fig. 8(a)] and an antenna [Fig. 8(b)]. For both detectors, the backscattered signal decreases with frequency. The antenna signal, however, drops faster than that detected by the photometric pixel. The signal detected by the antenna is indeed proportional to the wavelength squared, while the signal detected by the photometric pixel is proportional to the product $\pi\theta_r^2 S_{\mathrm{pup}}$ that is constant all over the spectrum. The signal decrease for the photometric pixel only hails from the attenuation due to the atmosphere and the brownout.

The backscattered noise increases with frequency for both detector types. For the antenna, the proportionality with the

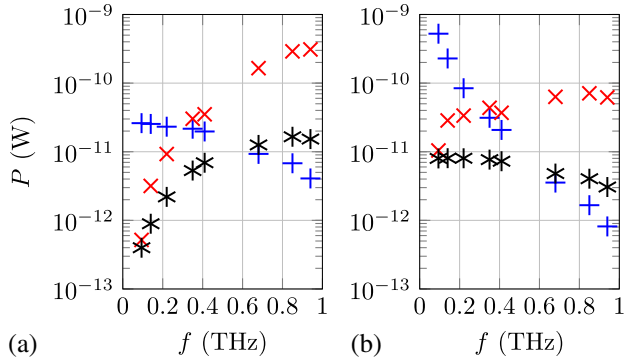

Fig. 8. Power balance for (a) a photometric pixel and (b) an antenna. The backscattered signal, the backscattered noise, and the thermal noise are, respectively, represented with +, ×, and ∗. Parameters: $P_0 = 1$ W, $\theta_0 = 25°$, $z_0 = 3$ m, $d_{s-c} = 0$, $p = 570$ µm, $\Delta f = 1$ GHz.

wavelength squared allows one to compensate for the increasing noise. As a result, the backscattered noise detected by the photometric detector grows faster than that of the antenna.

For the thermal noise, the compensation is even more powerful, as the thermal noise decreases for the antenna, while it intensifies for the photometric pixel. Besides, the power detected by a photometric pixel increases by more than 1 order of magnitude.

5. DISCUSSION

Figures 8(a) and 8(b) show the evolution of the difference in the detected powers for the photometric pixel and the antenna. These figures are nonetheless only accurate when the wavelength is smaller than twice the pixel pitch, or equivalently, for $f \geq f_{\text{lim}} = 260$ GHz. Below this frequency, the antenna would be subwavelength-sized, as the pixel pitch is assumed to be equal to 570 μm all over the spectrum. Such antennas are hard to design and even if they exist, the power balance would be valid for a single antenna, as the mutual coupling is not taken into account in our model. Below f_{lim}, the power balance for the photometric pixel is not valid, because such a detector is optimized as a flux sensor with a typical size larger than the wavelength.

In our model, we do not take into account the polarization of the antenna. Let us assume that the source is polarized perpendicularly to the detectors. While the Lambertian ground would depolarize the signal, the brownout would not depolarize the backscattered noise. Thus, the signal would be divided by 2, whereas the backscattered noise would be close to 0. The particles in suspension are indeed small compared to the wavelength, and the global scattering follows Rayleigh approximation.

Since the objective is to make an image through the brownout, a critical parameter is the contrast. We assume the ground albedo is $A_g = 0.1$, and a target of albedo $A_t = 0.05$ is in the scene. The contrast is defined as

$$\gamma = \frac{P_{\text{tot}}(A_g) - P_{\text{tot}}(A_t)}{P_{\text{tot}}(A_g) + P_{\text{tot}}(A_t)}, \tag{17}$$

where $P_{\text{tot}} = P_s + P_{\text{bs}} + P_g + P_{\text{sky}}$.

In a first approximation, the thermal noise detected by the antenna is proportional to the central wavelength squared. The ratio between the total detected power for an antenna and the radiance is thus constant. As a result, both sensor types present the same contrast. Considering the thermal noise to be negligible compared to the other powers, the maximum contrast is $\gamma_{\max} = (A_g - A_t)/(A_g + A_t) \approx 33\%$.

In order to lower the backscattered noise with respect to the backscattered signal, a solution is to use a bistatic system instead of a monostatic one. If the source and the detector are set apart by a distance d_{s-c} negligible compared to the brownout thickness D, the signal does not change much, whereas the backscattered noise decreases. In Figs. 9(a) and 9(b), we compare the contrast between a monostatic and a bistatic system. If we consider that the brownout is in direct contact with the optical system ($z_0 = 0$), we observe that the contrast is larger for a bistatic system than for a monostatic one. When z_0 grows, the contrast performance of a bistatic system is similar to a monostatic one.

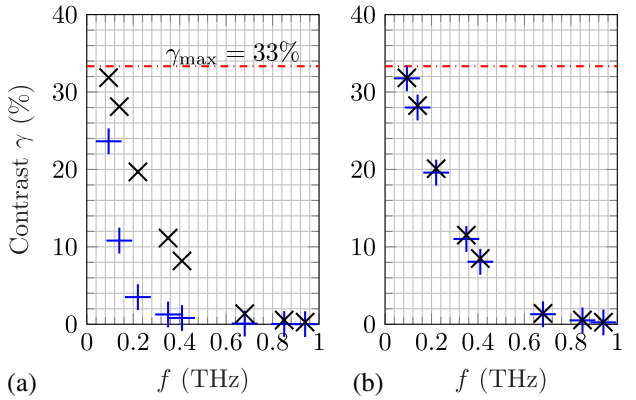

Fig. 9. Comparison of the contrasts between a monostatic ($d_{s-c} = 0$, +) and a bistatic ($d_{s-c} = 1$ m, ×) system and for two values of z_0. Parameters: $V = 30$ m, $D = 30$ m, $P_0 = 1$ W, $\theta_0 = 25°$, $p = 570$ μm. (a) $z_0 = 0$. (b) $z_0 = 3$ m.

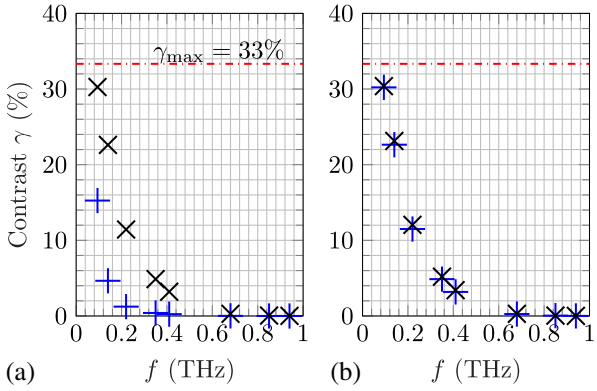

Fig. 10. Comparison of the contrasts between a monostatic ($d_{s-c} = 0$, +) and a bistatic ($d_{s-c} = 1$ m, ×) system and for two values of z_0. Parameters: $V = 10$ m, $D = 30$ m, $P_0 = 1$ W, $\theta_0 = 25°$, $p = 570$ μm. (a) $z_0 = 0$. (b) $z_0 = 3$ m.

Let us consider the visibility V_{pilot} defined in Section 3.C. With the parameters considered all along in this study, and particularly in Fig. 9, the visibility is 30 m. For the studies of propagation through degraded visual environment, the visibility is usually 10 m [32]. To have the same visibility and comparable results, we artificially increase the total density of particles ρ by a factor close to 3. For this visibility of 10 m, we show in Fig. 10 the contrast for a monostatic and a bistatic system and for different z_0. Similar to Fig. 9, the gain in performance for a bistatic system compared to a monostatic one when z_0 is greater than 0 m is low. For both visibilities, with a bistatic system and at low frequencies, we can reach similar contrasts close to 30%. Nonetheless, and unsurprisingly, we can observe that the contrast decreases much faster for a visibility V of 10 m than for 30 m.

6. CONCLUSION

A model has been proposed to determine the performance of an active subTHz imaging system in brownout conditions. First,

we determined analytically the main contributions to the power, that is to say, the backscattered signal, the backscattered noise, and the thermal noise. These solutions allowed us, on the one hand, to confirm the convergence and validity of Monte Carlo simulation, and on the other hand, to give a faster alternative resolution of the power balance. The distance between the imaging system and the brownout, z_0, is revealed to be crucial, as it is decisive for the choice between a monostatic or a bistatic system (Fig. 9).

Even if the backscattered noise is larger than the signal on a broad spectrum range, the necessary sensor dynamic to discriminate the signal from the background noise seems reachable. In the low part of the spectrum (up to 410 GHz), the physical properties do not seem to be a barrier to image through brownouts. A polarized imaging system could increase the contrast significantly. One must keep in mind that we had to choose a typical brownout that does not represent every brownout. However, we can assume our model of brownout is one of the worst cases for two reasons. First, the particle density was based on measurement for which the ground was tilled so as to maximize the flying particles [28]. The maximum altitude of measurement was 7 m and with a decreasing density with altitude while we assume here a 30-m-thick brownout of constant density. Thus, the density we used is *a priori* higher than brownout in real conditions. Second, we use the refractive index of silica, which is presumably higher than for real sand grains [6,21]. The scattering efficiency increases with the difference between the refractive indices of the particles and the atmosphere. Thus, in real conditions, the backscattering noise would be less important and the signal less attenuated.

Eventually, the challenge remains in the THz technology that needs to be developed. A powerful source combined with a dynamic and selective sensor is required to overcome the thermal and the backscattered noise.

APPENDICES

In these appendices, we present the analytical method to determine the signal backscattered by the scene to be imaged, L_s, and the noise backscattered by the suspended particles of the brownout, L_d.

APPENDIX A: RTE

In a scattering medium such as a brownout, the radiance L ($\mathrm{W \cdot m^{-2} \cdot sr^{-1}}$), at the position $\mathbf{r}$ and in direction defined by the unit vector $\hat{\mathbf{u}}$, follows the RTE:

$$\hat{\mathbf{u}} \cdot \nabla L(\mathbf{r}, \hat{\mathbf{u}}) + \frac{1}{\ell_{\mathrm{tot}}} L(\mathbf{r}, \hat{\mathbf{u}}) = \frac{1}{4\pi \ell_{\mathrm{sca}}} \int_{4\pi} p(\hat{\mathbf{u}}' \to \hat{\mathbf{u}}) L(\mathbf{r}, \hat{\mathbf{u}}') \mathrm{d}\hat{\mathbf{u}}' + S_0(\mathbf{r}, \hat{\mathbf{u}}), \quad \textbf{(A1)}$$

where $p(\hat{\mathbf{u}}' \to \hat{\mathbf{u}})$ is the scattering phase function from direction $\hat{\mathbf{u}}'$ to direction $\hat{\mathbf{u}}$. By definition, $\int_{4\pi} p(\hat{\mathbf{u}}' \to \hat{\mathbf{u}}) \mathrm{d}\hat{\mathbf{u}}' = 4\pi$. $S_0(\mathbf{r}, \hat{\mathbf{u}})$ is the source term due to the emitting antenna. ℓ_{tot} is the extinction mean free path that comprises the water absorption of the atmosphere and the scattering and absorption of the brownout particles. ℓ_{sca} is the scattering mean free path of the brownout particles. More precisely, we have

$$\frac{1}{\ell_{\mathrm{tot}}} = \frac{1}{\ell_{\mathrm{atm}}} + \frac{1}{\ell_{\mathrm{sca}}} + \frac{1}{\ell_{\mathrm{abs}}}. \quad \textbf{(A2)}$$

The radiance can be decomposed as the sum of the nonscattered field, L_s, and a scattered one, L_d, i.e.,

$$L(\mathbf{r}, \hat{\mathbf{u}}) = L_s(\mathbf{r}, \hat{\mathbf{u}}) + L_d(\mathbf{r}, \hat{\mathbf{u}}). \quad \textbf{(A3)}$$

APPENDIX B: NONSCATTERED RADIANCE

The nonscattered radiance is the solution of

$$\hat{\mathbf{u}} \cdot \nabla L_s(\mathbf{r}, \hat{\mathbf{u}}) + \frac{1}{\ell_{\mathrm{tot}}} L_s(\mathbf{r}, \hat{\mathbf{u}}) = S_0(\mathbf{r}, \hat{\mathbf{u}}). \quad \textbf{(B1)}$$

For an antenna of emission gain G_s and power P_0, the source term is

$$\mathcal{S}_0(\mathbf{r}, \hat{\mathbf{u}}) = \frac{G_s(-\hat{\mathbf{u}}) P_0}{4\pi \cos\theta_{\hat{\mathbf{u}}}} \delta(\mathbf{r}), \quad \textbf{(B2)}$$

where $\cos\theta_{\hat{\mathbf{u}}}$ is the projection of the radiance direction on the direction of the main lobe of the emission antenna. $\delta(\mathbf{r})$ is the Dirac delta function that expresses that the source antenna is located at the position $\mathbf{r} = \mathbf{0}$.

It has been shown that the solution of Eq. (B1) can be written using the Green function $\mathcal{G}_0$ [34]:

$$L_s(\mathbf{r}, \hat{\mathbf{u}}) = \int_V \mathcal{G}_0(\mathbf{r} - \mathbf{r}', \hat{\mathbf{u}}) S_0(\mathbf{r}', \hat{\mathbf{u}}) \mathrm{d}\mathbf{r}', \quad \textbf{(B3)}$$

with

$$\mathcal{G}_0(\mathbf{r}, \hat{\mathbf{u}}) = \frac{\exp(-r/\ell_{\mathrm{tot}})}{r^2} \delta(\hat{\mathbf{u}} + \hat{\mathbf{r}}). \quad \textbf{(B4)}$$

We deduce the radiance in the medium, before any backscattering by the scene:

$$L_s(\mathbf{r}, \hat{\mathbf{u}}) = \frac{G_s(-\hat{\mathbf{u}}) P_0}{4\pi |\mathbf{r}|^2 \cos\theta_{\hat{\mathbf{u}}}} \exp\left(-\frac{|\mathbf{r}|}{\ell_{\mathrm{tot}}}\right) \delta\left(\hat{\mathbf{u}} + \frac{\mathbf{r}}{|\mathbf{r}|}\right). \quad \textbf{(B5)}$$

APPENDIX C: BACKSCATTERED SIGNAL

The radiance that is incident on the pupil hails from a small scene portion that is proportional to the pixel aperture. This area is assumed negligible, so that the irradiance at this point area of coordinates $\mathbf{d}'_{\mathbf{s-c}} = d_{s-c}\hat{\mathbf{x}} + D\hat{\mathbf{z}}$ is

$$E_s(\mathbf{r}'_{\mathbf{0}}) = \int_{4\pi} L_s(\mathbf{r}'_{\mathbf{0}}, \hat{\mathbf{u}}) \cos\theta_{\hat{\mathbf{u}}} \mathrm{d}\hat{\mathbf{u}}. \quad \textbf{(C1)}$$

d_{s-c} is negligible compared to $D + z_0$ and $1/\ell_{\mathrm{atm}} \approx 1/\ell_{\mathrm{tot}}$. Thus,

$$E_s(\mathbf{r}'_{\mathbf{0}}) = \frac{P_0 G_s(\hat{\mathbf{z}})}{4\pi (D + z_0)^2} \exp\left(-\frac{D + z_0}{\ell_{\mathrm{tot}}}\right). \quad \textbf{(C2)}$$

The ground is Lambertian of albedo A_g so that the radiance backscattered by the ground is proportional to A_g/π. The pupil radius, $\Phi/2$, is negligible compared to the distance between the optical system and the scene so that the radiance incident on the pupil is assumed uniform. The pixel aperture is so small that the radiance from the ground is only detected along the $-\hat{\mathbf{z}}$ direction. The radiance on the pupil is finally

$$L_s^r = \frac{A_g G_s(\hat{\mathbf{z}}) P_0}{4\pi^2 (D + z_0)^2} \exp\left(-\frac{2(D + z_0)}{\ell_{\mathrm{tot}}}\right). \quad \textbf{(C3)}$$

APPENDIX D: SCATTERED RADIANCE

For the scattered radiance, L_d, the RTE [Eq. (A1)] is simplified as follows:

$$\hat{\mathbf{u}}\cdot\nabla L_d(\mathbf{r},\hat{\mathbf{u}})+\frac{1}{\ell_{\text{tot}}}L_d(\mathbf{r},\hat{\mathbf{u}}) =\frac{1}{4\pi\ell_{\text{sca}}}\int_{4\pi}p(\hat{\mathbf{u}}'\to\hat{\mathbf{u}})L(\mathbf{r},\hat{\mathbf{u}}')\mathrm{d}\hat{\mathbf{u}}'. \tag{D1}$$

As the brownout thickness is negligible compared to the scattering mean free path, we assume the wave propagation is in the single-scattering regime. Therefore, only L_s can be scattered. and the RTE becomes

$$\hat{\mathbf{u}}\cdot\nabla L_d(\mathbf{r},\hat{\mathbf{u}})+\frac{1}{\ell_{\text{tot}}}L_d(\mathbf{r},\hat{\mathbf{u}}) =\frac{1}{4\pi\ell_{\text{sca}}}\int_{4\pi}p(\hat{\mathbf{u}}'\to\hat{\mathbf{u}})L_s(\mathbf{r},\hat{\mathbf{u}}')\mathrm{d}\hat{\mathbf{u}}'. \tag{D2}$$

The last term of the equation can be considered as a source term S_d:

$$S_d(\mathbf{r},\hat{\mathbf{u}})=\frac{1}{4\pi\ell_{\text{sca}}}\int_{4\pi}p(\hat{\mathbf{u}}'\to\hat{\mathbf{u}})L_s(\mathbf{r},\hat{\mathbf{u}}')\mathrm{d}\hat{\mathbf{u}}'. \tag{D3}$$

Let us insert Eq. (B5) in Eq. (D3):

$$\mathcal{S}_d(\mathbf{r},\hat{\mathbf{u}})=\frac{1}{4\pi\ell_{\text{sca}}}\int_{4\pi}p(\hat{\mathbf{u}}'\to\hat{\mathbf{u}})\frac{G_s(-\hat{\mathbf{u}}')P_0}{4\pi|\mathbf{r}|^2\cos\theta_{\hat{\mathbf{u}}'}} \times\exp\left(-\frac{|\mathbf{r}|}{\ell_{\text{tot}}}\right)\delta\left(\hat{\mathbf{u}}'+\frac{\mathbf{r}}{|\mathbf{r}|}\right)\mathrm{d}\hat{\mathbf{u}}'. \tag{D4}$$

Let us note $\hat{\mathbf{r}}=\mathbf{r}/|\mathbf{r}|$:

$$\mathcal{S}_d(\mathbf{r},\hat{\mathbf{u}})=\frac{p(-\hat{\mathbf{r}}\to\hat{\mathbf{u}})}{4\pi\ell_{\text{sca}}}\frac{G_s(\hat{\mathbf{r}})P_0}{4\pi|\mathbf{r}|^2\cos\theta_{-\hat{\mathbf{r}}}}\exp\left(-\frac{|\mathbf{r}|}{\ell_{\text{tot}}}\right). \tag{D5}$$

Similar to Eq. (B3), a solution of Eq. (D2) is

$$L_d(\mathbf{r},\hat{\mathbf{u}})=\int_V\mathcal{G}_0(\mathbf{r}-\mathbf{r}',\hat{\mathbf{u}})S_d(\mathbf{r}',\hat{\mathbf{u}})\mathrm{d}\mathbf{r}', \tag{D6}$$

where V is the brownout volume, and $\mathcal{G}_0$ is the Green's function written below. The volume of integration V is the intersection volume of the cone of emission and the cone of detection.

Let us introduce the expression of $\mathcal{G}_0$ and S_d in Eq. (D6):

$$L_d(\mathbf{r},\hat{\mathbf{u}})=\frac{P_0}{(4\pi)^2\ell_{\text{sca}}}\int_V\frac{G_s(\hat{\mathbf{r}}')}{\cos(\theta_{-\hat{\mathbf{r}}'})}\frac{p(-\hat{\mathbf{r}}'\to\hat{\mathbf{u}})}{|\mathbf{r}-\mathbf{r}'|^2|\mathbf{r}'|^2} \times\exp\left(-\frac{|\mathbf{r}-\mathbf{r}'|+|\mathbf{r}'|}{\ell_{\text{tot}}}\right)\delta\left(\hat{\mathbf{u}}+\frac{\mathbf{r}-\mathbf{r}'}{|\mathbf{r}-\mathbf{r}'|}\right)\mathrm{d}\mathbf{r}', \tag{D7}$$

where $\hat{\mathbf{r}}'=\mathbf{r}'/|\mathbf{r}'|$.

APPENDIX E: IRRADIANCE OF THE BACKSCATTERED NOISE

The backscattered irradiance received on the imaging system, E_d^r, is given by

$$E_d^r(\mathbf{r})=\int_{4\pi}L_d(\mathbf{r},\hat{\mathbf{u}})\cos\theta_{\hat{\mathbf{u}}}\mathrm{d}\hat{\mathbf{u}}, \tag{E1}$$

where $\mathbf{r}$ is the position on the pupil located in the plane of equation $z=0$.

The detection system is highly directive so that $\cos\theta_{\hat{\mathbf{u}}}\approx 1$. Using Eq. (D7), we get

$$E_d(\mathbf{r}_{\text{pup}})=\frac{P_0}{(4\pi)^2\ell_{\text{sca}}}\int_V\frac{G_s(\hat{\mathbf{r}}')}{\cos(\theta_{-\hat{\mathbf{r}}'})}\frac{p(-\hat{\mathbf{r}}'\to-\hat{\mathbf{r}}'_{\text{pup}})}{|\mathbf{r}_{\text{pup}}-\mathbf{r}'|^2|\mathbf{r}'|^2} \times\exp\left(-\frac{|\mathbf{r}_{\text{pup}}-\mathbf{r}'|+|\mathbf{r}'|}{\ell_{\text{tot}}}\right)\mathrm{d}\mathbf{r}', \tag{E2}$$

with $\hat{\mathbf{r}}'_{\text{pup}}=(\mathbf{r}_{\text{pup}}-\mathbf{r}')/|\mathbf{r}_{\text{pup}}-\mathbf{r}'|$.

A. Exact Resolution of Eq. (E2)

We implement the integration in spherical coordinates ($d\mathbf{r}'=|\mathbf{r}'|^2dr'd\hat{\mathbf{r}}'$):

$$E_d(\mathbf{r}_{\text{pup}})=\frac{P_0}{(4\pi)^2\ell_{\text{sca}}}\int_{4\pi}\frac{G_s(\hat{\mathbf{r}}')p(-\hat{\mathbf{r}}'\to-\hat{\mathbf{r}}'_{\text{pup}})}{\cos(\theta_{-\hat{\mathbf{r}}'})} \times\left\{\int_{r_1(\hat{\mathbf{r}}')}^{r_2(\hat{\mathbf{r}}')}\frac{\exp(-(|\mathbf{r}_{\text{pup}}-\mathbf{r}'|+|\mathbf{r}'|)/\ell_{\text{tot}})}{|\mathbf{r}_{\text{pup}}-\mathbf{r}'|^2}\mathrm{d}r'\right\}\mathrm{d}\hat{\mathbf{r}}'. \tag{E3}$$

Here, r_1 and r_2 are the points of entry and exit in the intersection volume V, along the direction $\hat{\mathbf{r}}'$.

We assume the particles are spherical so that the phase function only depends on $\hat{\mathbf{r}}_{\mathbf{0}'}\cdot\hat{\mathbf{r}}'$. We assume the backscattering angle is small so that $p(-\hat{\mathbf{r}}'\to-\hat{\mathbf{r}}'_{\text{pup}})\approx p(\hat{\mathbf{u}}\to-\hat{\mathbf{u}})$.

We introduce the backscattering length defined by $\ell_{\text{bs}}=4\pi\ell_{\text{sca}}/p(\hat{\mathbf{u}}\to-\hat{\mathbf{u}})$:

$$E_d(\mathbf{r}_{\text{pup}})=\frac{P_0}{4\pi\ell_{\text{bs}}}\int_{4\pi}\frac{G_s(\hat{\mathbf{r}}')}{\cos(\theta_{-\hat{\mathbf{r}}'})}\{\mathcal{F}(\mathbf{r}_{\text{pup}},r_2(\hat{\mathbf{r}}')) -\mathcal{F}(\mathbf{r}_{\text{pup}},r_1(\hat{\mathbf{r}}'))\}\mathrm{d}\hat{\mathbf{r}}', \tag{E4}$$

with the primitive $\mathcal{F}(\mathbf{y},\mathbf{x})$,

$$\mathcal{F}(\mathbf{y},\mathbf{x})=\frac{i}{2|\mathbf{y}|\sin\theta'}\exp\left(-\frac{2|\mathbf{y}|e^{i\theta'}}{\ell_{\text{tot}}}\right) \times\left\{\exp\left(\frac{4i|\mathbf{y}|\sin\theta'}{\ell_{\text{tot}}}\right)\mathbf{Ei}\left[-\frac{2(|\mathbf{x}|-|\mathbf{y}|e^{-i\theta'})}{\ell_{\text{tot}}}\right] -\mathbf{Ei}\left[-\frac{2(|\mathbf{x}|-|\mathbf{y}|e^{i\theta'})}{\ell_{\text{tot}}}\right]\right\}, \tag{E5}$$

where i is the imaginary unit and $\mathbf{Ei}$ is the exponential integral function.

B. Resolution of Eq. (E2) with Small Angle Approximation

We present here the results of Eq. (E2) with small angle approximation. The cones of illumination and detection are considered along their main axis $\hat{\mathbf{z}}$. The integration is thus done in cylindrical coordinates. We assume that the section of the intersection volume V at the depth z is negligible compared to z. In other words, $d\mathbf{r}'=|\mathbf{r}'|^2dr'd\hat{\mathbf{r}}'\approx z'^2dz\Omega_{\text{pix}}$. At the depth z, the system images a section of the brownout approximately equal to S_{pup} and that is partially illuminated by the source. The illuminated section has an area $S_\cap(z)$, intersection of the illumination, and the detection cones at depth z. The radiation of the brownout section that is not illuminated by the source is negligible or even null. Thus, we can write

$$E_d(\mathbf{d_{s-c}}) = \frac{P_0 \Omega_{\text{pix}} G_s}{4\pi \ell_{\text{bs}}} \int_{z_0}^{D+z_0} \frac{S_\cap(z')}{S_{\text{pup}}} \times \frac{\exp\left(-\left(\sqrt{d_{s-c}^2 + z'^2} + z'\right)/\ell_{\text{tot}}\right)}{d_{s-c}^2 + z'^2} \mathrm{d}z', \quad \textbf{(E6)}$$

with the gain of the emission antenna $G_s = 2/(1 - \cos\theta_0)$.

Funding. Safran Electronics & Defense; Direction Générale de l'Armement (DGA); Labex WIFI (ANR-10-IDEX-0001-02 PSL, ANR-10-LABX-24).

REFERENCES

1. A. Davis, "The use of commercial remote sensing predicting helicopter brownout conditions," Master's thesis (Naval Postgraduate School, 2007), http://www.dtic.mil/dtic/tr/fulltext/u2/a473870.pdf.
2. D. A. Wachspress, G. R. Whitehouse, J. D. Keller, K. Yu, P. Gilmore, M. Dorsett, and K. McClure, "A high fidelity brownout model for real-time flight simulations and trainers," presented at the American Helicopter Society 65th Annual Forum, Grapevine, Texas, 2009.
3. B. A. Swanson, "Investigating the impacts of particle size and wind speed on brownout," Master's thesis (Air Force Institute of Technology, 2015), http://www.dtic.mil/dtic/tr/fulltext/u2/a614925.pdf.
4. R. C. Allen, W. B. Blanton, E. Schramm, and R. Mitra, "Strategies for reducing SWAP-C and complexity in DVE sensor systems," Proc. SPIE **10197**, 101970M (2017).
5. A. Stambler, S. Spiker, M. Bergerman, and S. Singh, "Toward autonomous rotorcraft flight in degraded visual environments: experiments and lessons learned," Proc. SPIE **9839**, 983904 (2016).
6. S. T. Fiorino, P. M. Grice, M. J. Krizo, R. J. Bartell, J. D. Haiducek, and S. J. Cusumano, "Lab measurements to support modeling terahertz propagation in brownout conditions," Proc. SPIE **7671**, 76710W (2010).
7. M. Hagelen, G. Briese, H. Essen, T. Bertuch, P. Knott, and A. Tessmann, "A millimetrewave landing aid approach for helicopters under brown-out conditions," in *IEEE Radar Conference* (IEEE, 2008), pp. 1–4.
8. H. O. Everitt, W. D. Caraway, and J. T. Richard, "Terahertz (THz) radar: a solution for degraded visibility environments (DVE)," Technical Report TR-RDMR-WD-16-49 (Army Research, Development and Engineering Command Redstone Arsenal United States, 2016).
9. T. E. Dillon, C. A. Schuetz, R. D. Martin, D. G. Mackrides, S. Shi, P. Yao, K. Shreve, C. Harrity, and D. W. Prather, "Passive, real-time millimeter wave imaging for degraded visual environment mitigation," Proc. SPIE **9471**, 947103 (2015).
10. A. Wright, R. Martin, C. Schuetz, S. Shi, Y. Zhang, P. Yao, K. Shreve, T. E. Dillon, D. G. Mackrides, C. E. Harrity, and D. W. Prather, "Module integration and amplifier design optimization for optically enabled passive millimeter-wave imaging," Proc. SPIE **9830**, 98300C (2016).
11. S. Sarkozy, J. Drewes, K. M. Leong, R. Lai, X. G. Mei, W. Yoshida, M. D. Lange, J. Lee, and W. R. Deal, "Amplifier based broadband pixel for sub-millimeter wave imaging," Opt. Eng. **51**, 091602 (2012).
12. V. Radisic, K. Leong, C. Zhang, K. K. Loi, and S. Sarkozy, "Demonstration of a micro-integrated sub-millimeter-wave pixel," IEEE Trans. Microwave Theory Tech. **61**, 2949–2955 (2013).
13. M. I. B. Shams, Z. Jiang, S. Rahman, J. Qayyum, L. J. Cheng, H. G. Xing, P. Fay, and L. Liu, "Approaching real-time terahertz imaging with photo-induced coded apertures and compressed sensing," Electron. Lett. **50**, 801–803 (2014).
14. C. A. Schuetz, E. L. Stein, J. Samluk, D. Mackrides, J. P. Wilson, R. D. Martin, T. E. Dillon, and D. W. Prather, "Studies of millimeter-wave phenomenology for helicopter brownout mitigation," Proc. SPIE **7485**, 74850F, 2009.
15. D. Wikner, "Millimeter-wave propagation through a controlled dust environment," Proc. SPIE **6548**, 654803 (2007).
16. R. Ceolato, B. Tanguy, C. Martin, T. Huet, P. Chervet, G. Durand, N. Riviere, L. Hespel, N. Diakonova, D. But, W. Knap, J. Meilhan, B. Delplanque, J. Oden, and F. Simoens, "Performance evaluation of active sub-terahertz systems in degraded visual environments (DVE)," Proc. SPIE **9839**, 983906 (2016).
17. C. Phillips, Computational Study of Rotorcraft Aerodynamics in Ground Effect and Brownout (Defense Advanced Research Projects Agency, 2010).
18. K. Sudhakar and M. V. Subramanyam, "Evaluation of atmospheric attenuation due to various parameters," in *International Conference on Information Communication and Embedded Systems (ICICES)* (IEEE, 2013), pp. 609–612.
19. K. Sudhakar and M. Subramanyam, "Propagation power loss analysis and evaluation under variant atmospheric conditions," Glob. J. Res. Eng. **13**, 17–20 (2013).
20. R. Ceolato, N. Diakonova, J. Meilhan, and W. Knap, "Determination of the sub-terahertz attenuation of brownout clouds generated by rotorcraft," in *42nd International Conference on Infrared, Millimeter, and Terahertz Waves (IRMMW-THz)* (IEEE, 2017), pp. 1–2.
21. S. L. Marek, "A computational tool for evaluating THz imaging performance in brownout conditions at land sites throughout the world," Master's thesis (Air Force Institute of Technology, 2009), http://www.dtic.mil/dtic/tr/fulltext/u2/a494962.pdf.
22. S. T. Fiorino, R. J. Bartell, M. J. Krizo, S. L. Marek, M. J. Bohn, R. M. Randall, and S. J. Cusumano, "A computational tool for evaluating THz imaging performance in brownout or whiteout conditions at land sites throughout the world," Proc. SPIE **7324**, 732410 (2009).
23. V. Belov, "Statistical modeling of imaging process in active night vision systems with gate-light detection," Appl. Phys. B **75**, 571–576 (2002).
24. V. V. Belov, V. N. Abramochkin, Y. V. Gridnev, A. N. Kudryavtsev, V. S. Kozlov, R. F. Rakhimov, V. P. Shmargunov, and M. V. Tarasenkov, "Experimental study of the influence of optical characteristics of a medium on the image quality in optoelectronic systems with backscattered noise signal selection," Atmos. Ocean. Opt. **30**, 429–434 (2017).
25. J. M. Hammersley and D. C. Handscomb, *Monte Carlo Methods* (Chapman & Hall, 1964).
26. G. S. Fishman, *Monte Carlo Concepts, Algorithms and Applications* (Springer-Verlag, 1996).
27. Radiocommunication Sector ITU, "Recommendation ITU-R P. 676–11: attenuation by atmospheric gases," Technical Report ITU-R P.676-11 (International Telecommunication Union, 2016).
28. C. Cowherd, "Sandblaster 2 support of see-through technologies for particulate brownout," Technical Report 110565 (Midwest Research Institute, 2007).
29. H. van de Hulst, *Light Scattering by Small Particles* (Dover Publications, 1981).
30. H. Koschmieder, "Measurements of visibility at Danzig," Mon. Weather Rev. **58**, 439–444 (1930).
31. W. E. K. Middleton, *Vision Through the Atmosphere* (Springer Berlin Heidelberg, 1957), pp. 254–287.
32. D. W. Prather, N. Alexander, R. Appleby, C. Callejero, R. Gonzalo, D. Nötel, N. Salmon, B. Wallace, M. Peichl, and C. Schuetz, "High-performance passive/active radiometric mmw imaging using thinned arrays (set-135)," Technical Report STO-TR-SET-135 (NATO, 2015).
33. F. Taillade, E. Belin, and E. Dumont, "An analytical model for backscattered luminance in fog: comparisons with Monte Carlo computations and experimental results," Meas. Sci. Technol. **19**, 055302 (2008).
34. A. Marshak and A. Davis, *3D Radiative Transfer in Cloudy Atmospheres* (Springer, 2005), Chap. 3, p. 213.